Received: 11 October 2022 | Revised: 28 February 2023 | Accepted: 5 March 2023

DOI: 10.1002/bit.28372

ARTICLE

BIOTECHNOLOGY AND BIOENGINEERING WILEY

Scale-down of oxygen and glucose fluctuations in a tubular photobioreactor operated under oxygen-balanced mixotrophy

Pedro Moñino Fernández | Albert Vidal García | Tanisha Jansen | Wendy Evers | Maria Barbosa | Marcel Janssen

Bioprocess Engineering, AlgaePARC, Wageningen University and Research, Wageningen, The Netherlands

Correspondence
Pedro Moñino Fernández
Email: pedro.moninofernandez@wur.nl

Funding information
Horizon 2020 Framework Programme

Abstract

Oxygen-balanced mixotrophy (*OBM*) is a novel type of microalgal cultivation that improves autotrophic productivity while reducing aeration costs and achieving high biomass yields on substrate. The scale-up of this process is not straightforward, as nonideal mixing in large photobioreactors might have unwanted effects in cell physiology. We simulated at lab scale dissolved oxygen and glucose fluctuations in a tubular photobioreactor operated under *OBM* where glucose is injected at the beginning of the tubular section. We ran repeated batch experiments with the strain *Galdieria sulphuraria* ACUF 064 under glucose pulse feeding of different lengths, representing different retention times: 112, 71, and 21 min. During the long and medium tube retention time simulations, dissolved oxygen was depleted 15–25 min after every glucose pulse. These periods of oxygen limitation resulted in the accumulation of coproporphyrin III in the supernatant, an indication of disruption in the chlorophyll synthesis pathway. Accordingly, the absorption cross-section of the cultures decreased steeply, going from values of 150–180 $m^2\ kg^{-1}$ at the end of the first batch down to 50–70 $m^2\ kg^{-1}$ in the last batches of both conditions. In the short tube retention time simulation, dissolved oxygen always stayed above 10% air saturation and no pigment reduction nor coproporphyrin III accumulation were observed. Concerning glucose utilization efficiency, glucose pulse feeding caused a reduction of biomass yield on substrate in the range of 4%–22% compared to the maximum levels previously obtained with continuous glucose feeding (0.9 C-g C-g^{-1}). The missing carbon was excreted to the supernatant as extracellular polymeric substances constituted by carbohydrates and proteins. Overall, the results point out the importance of studying large-scale conditions in a controlled environment and the need for a highly controlled glucose feeding strategy in the scale-up of mixotrophic cultivation.

KEYWORDS

coproporphyrin III, extracellular polymeric substance, *Galdieria sulphuraria*, oxygen limitation, oxygen-balanced mixotrophy, scale-down

1 | INTRODUCTION

Microalgae are considered a promising feedstock in the transition towards sustainable production systems and the biobased economy (Fernández et al., 2021). These unicellular photoautotrophic (from now on: autotrophic) organisms initially raised considerable interest due to their natural ability to fix atmospheric carbon dioxide (CO_2) at higher rates than land plants (Chelf et al., 1993). Nevertheless, the development of large-scale autotrophic cultivation has been restrained by a number of factors that limit the economic feasibility of bulk products (Janssen et al., 2022; Khan et al., 2018). Carbon fixation is dependent on light availability, but light penetration is poor in concentrated cultures due to mutual cell shading. A common practice to circumvent this problem usually involves reactor operation at low biomass concentration, incurring higher downstream processing costs. Besides light limitation, microalgal cell growth might also be limited by an insufficient supply of CO_2 and accumulation of oxygen (O_2). For this reason, ensuring an adequate gas–liquid transfer is essential to avoid suboptimal productivities. This is usually approached in two ways: CO_2-enriched gas supply and high aeration flow rates, both having an impact in the final costs of the process (Langley et al., 2012; Ruiz et al., 2016).

A strategy to tackle the yet elevated production costs of autotrophic cultivation consists of the addition of organic carbon substrates to illuminated microalgal cultures (Pang et al., 2019). In this way, autotrophic metabolism is combined with the heterotrophic counterpart in a mixotrophic regime. Light dependency is reduced as growth can proceed in the dark zones of the reactor. This increases productivity and biomass concentration at the expense of the organic carbon source, while maintaining the possible benefits of autotrophic carbon fixation. If substrate supply is adjusted to match photosynthetic oxygen production, then oxygen consumption and production can be balanced by means of intracellular "gas recycling" (Grama et al., 2016). Most CO_2 resulting from the oxidation of the substrate is, in turn, fixed by the photosynthetic machinery, achieving up to 90% efficiency in the utilization of the organic carbon. Altogether, this type of mixotrophy, denominated *OBM*, enables to operate photobioreactors without any gas exchange during daylight, obtain higher biomass concentration and achieve maximal carbon conversion efficiency (Abiusi et al., 2020a, 2020b, 2021, 2022).

So far, we have successfully developed *OBM* in a lab-scale reactor, constituted by a cylindrical vessel with a working volume of 2 L and mechanical stirring at 500 rpm (Abiusi et al., 2020a). Such system can be considered ideally mixed, meaning that the concentrations of biomass, organic substrate, and dissolved oxygen (*DO*) are virtually the same in the entire volume. When the organic carbon source is supplied, it is almost immediately depleted after becoming in contact with the liquid. In this manner, a stable *DO* level is achieved while maintaining organic substrate concentration close to 0. On the other hand, in larger systems, mixing is far from ideal. For example, one of the most common reactor configurations for large-scale cultivation of microalgae is tubular photobioreactors, characterized by plug flow fluid dynamics (Acién Fernández et al., 2001). Based on the combination of this type of fluid behavior and algal growth, both oxygen and organic substrate gradients are expected along the tubes. Achieving oxygen balance in such scenario might thus be more complex than at lab-scale. Accordingly, the algal cells might experience a changing environment with unknown effects on their mixotrophic metabolic equilibrium, entailing a scale-up risk for this process.

The aim of this work was to evaluate the performance of *OBM* in tubular photobioreactors before carrying out the actual scale-up. This issue was tackled by developing a scale-down strategy that reproduced mixotrophy in a tubular photobioreactor. Scale-down strategies are a common procedure in heterotrophic bioprocesses (Noorman, 2011) and have also been applied in tubular photobioreactors operated autotrophically (Rosello Sastre et al., 2007), but never mixotrophically. The idea behind is to mimic large-scale fluctuating conditions in a lab-scale setup, mainly focusing on sugar and oxygen availability. This allows to gain understanding about the physiological response of the cells in a changing environment and how that affects the overall performance of the process. The information gathered can then be used to derisk the subsequent scale-up design. Our approach consisted of feeding glucose in pulses of different length, creating gradients of oxygen and organic carbon substrate that resembled those expected in a tubular photobioreactor. Consistently with our previous research, we chose *Galdieria sulphuraria* for this study as its acidophilic nature prevents bacterial growth, a great advantage in a mixotrophic cultivation system with an organic carbon source (Abiusi et al., 2021, 2022). As such, we consider this species as an ideal candidate for the scale-up of *OBM*.

2 | MATERIALS AND METHODS

2.1 | Strain, inoculum cultivation, and medium

G. sulphuraria ACUF 064 (http://www.acuf.net) was kindly donated by Prof. A. Pollio (University of Naples, Italy). Cryopreserved cells were defrosted and cultivated axenically in 250-mL flasks containing 100 mL of medium at 37°C, 2% v/v CO_2, 120 rpm, and under a photon flux density (*PFD*) of 75 µmol m^{-2} s^{-1}. These cultures were used to inoculate the photobioreactor for the experiments described below. The medium used for both flask and reactor cultivation was composed of the following (expressed in mol L^{-1}): 8.0×10^{-2} $(NH_4)_2SO_4$, 6.5×10^{-3} $MgSO_4 \cdot 7H_2O$, 4.7×10^{-4} $CaCl_2 \cdot 2H_2O$, 6.3×10^{-4} ethylenediaminetetraacetic acid (EDTA) ferric sodium salt, 2.0×10^{-4} EDTA disodium salt dihydrate, 1.2×10^{-2} H_3PO_4, 1.7×10^{-3} NaCl, 8.1×10^{-3} KCl, 8.0×10^{-4} H_3BO_3, 8.1×10^{-5} $MnCl_2 \cdot 4H_2O$, 8.2×10^{-5} $ZnCl_2$, 3.2×10^{-5} $CuSO_4 \cdot 5H_2O$, 1.7×10^{-5} $Na_2MoO_4 \cdot 2H_2O$, and 1.7×10^{-5} $CoCl_2 \cdot 6H_2O$. pH was adjusted to 1.8 with 6 mL L^{-1} of 2 M H_2SO_4.

2.2 | Photobioreactor setup

Experiments were carried out in a 3-L stirred-tank bioreactor with an internal diameter of 0.13 m (Applikon). The liquid height was maintained

at 0.165 m, resulting in a working volume (V_{PBR}) of 2 L and a cylindrical illuminated surface (*IS*) of 0.067 m^2. The vessel was illuminated homogeneously with an average continuous *PFD* of 507 ± 45 µmol m^{-2} s^{-1}, as described in detail in Abiusi et al. (2020a). Continuous stirring at 500 rpm was applied during all experiments. The temperature was controlled at 37°C and water evaporation was prevented with a condenser fed with water at 2°C. pH was maintained at 1.8 by automatic base addition (2 M NaOH). *DO* was measured by a VisiFerm DO ECS 225 *DO* sensor (Hamilton). The sensor was calibrated inside the reactor containing medium at the aforesaid working temperature and pH. The temperature was automatically accounted for during the measurements by means of the built-in thermometer in the *DO* sensor. Pressure during calibration and subsequent reactor operation was slightly above atmospheric levels (<1% difference, data not shown). This difference was considered negligible when processing the measured data. Dinitrogen gas (N_2) and air sparging were applied to obtain 0% and 100% *DO* reads, respectively. During autotrophic and mixotrophic adaptation phases, the reactor was sparged with air enriched with 2% v/v CO_2 at a flow rate of 1 L min^{-1} using Smart TMF 5850 S mass flow controllers (Brooks Instruments). Volume increase due to glucose external supply and/or base addition was compensated by daily sampling.

2.3 | Repeated batch cultivation of *G. sulphuraria*

G. sulphuraria ACUF 064 was cultivated axenically in repeated batch in three different experimental conditions: short, medium, and long hydraulic retention time (*HRT*) simulation of a tubular reactor under *OBM*. At each condition, several consecutive batches were performed. The first batch started similarly in the three scenarios as an adaptation to the new conditions. First, the reactor was inoculated with an autotrophic culture at an initial biomass concentration (C_x) of 0.8 g L^{-1}. Then, the reactor was operated autotrophically for 3 days, followed by a mixotrophic adaptation phase of 2 days. During the latter, a glucose solution of 100 g L^{-1} was fed at a fixed rate of 1.0 ± 0.3 g solution h^{-1}. After this phase, aeration was switched off and *DO* was controlled at 90% air saturation by addition of 100 g L^{-1} glucose solution for 2 more days (i.e., adaptation to *OBM*). At this point, the cultures were diluted with fresh medium and the first batch finished. Thereafter, glucose was supplied in pulses to the reactor from the second batch until the last batch of each condition. In addition, these batches started always at a biomass concentration of 3 g L^{-1} and were carried for 4 days until the next dilution. These starting concentrations and batch duration were selected as optimal to stay within the linear growth range based on previous work (Abiusi et al., 2021). In total, five batches were carried for the long simulation and eight for the short and medium simulations, including the initial adaptation batch.

2.4 | Glucose pulse feeding

Glucose was supplied discontinuously to mimic the oxygen and substrate gradients experienced by the cells in a tubular reactor operated under *OBM*. The glucose pump was activated at its maximum rate (147 g h^{-1}) for a certain period of time (i.e., blockwise) when *DO* increased to 60% air saturation. This glucose pulse triggered an almost immediate increase in glucose concentration that drove oxygen below the setpoint of 60%, as depicted in Figure 1. This setpoint was selected based on preliminary trials that focused on maximizing response stability after the pulse and preventing setpoint deviation from air saturation levels (data not shown). The sudden increase in glucose concentration represents the cells passing by the beginning of the tube, where the organic substrate is fed. As the cells oxidized the glucose, oxygen decreased (i.e., cells moved through the simulated tube). When glucose was depleted, *DO* rose again triggering a new glucose pulse. The length of the glucose pulse determined the time between consecutive *DO* peaks. This time equals the *HRT* within the simulated tubular reactor, assuming (1) a single glucose feeding point at the beginning and (2) mixotrophic growth throughout the whole tube. The pumping times required for the long, medium, and short simulations were determined empirically by gradual adjustment of the pumping time at the beginning of batch 2. Once stable cycles of similar duration to the desired *HRT* were obtained, a fixed pumping time was kept during the rest of each experimental condition. The calculation of the *HRT* is explained in the next section. Occasionally, right after batch dilution, there was a *DO* spike (>100% air saturation) caused by the sudden increase in photon supply (Abiusi et al., 2021) that could not be controlled by pulse feeding. During these periods, glucose solution was fed at a fixed rate of 2.1 ± 0.1 g h^{-1} to maintain cell adaptation to mixotrophy. Once *DO* decreased below 100% air saturation, pulse feeding was resumed.

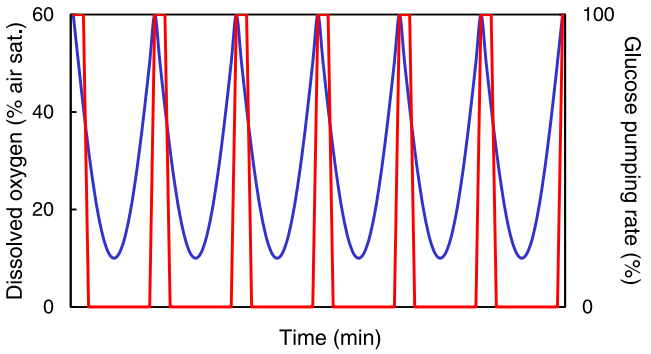

FIGURE 1 Schematic representation of the glucose pulse feeding strategy. Dissolved oxygen concentration (blue) and glucose pumping rates (red) are depicted in time. The relative size of the glucose pump rate has been exaggerated for the sake of visual representation.

2.5 | Retention time calculation

As a reference for the retention time simulation, we selected a tubular photobioreactor with a solar collector loop (*L*) of 300 m and an internal diameter (*d*) of 0.06 m. These are common dimensions for pilot scale tubular photobioreactors, such as the GemTube MK-1 1500 s tubular photobioreactor (Lgem) located at our AlgaePARC

greenhouse facility (Bennekom, the Netherlands), described elsewhere (Guimarães et al., 2021). In this study, three different *HRT* were simulated for such reactor: short, medium, and long. The long simulation aimed to reproduce the maximum *HRT* attainable in such system. That is, the system operated at the minimum liquid velocity possible. Under *OBM*, there is no oxygen accumulation, and thus the liquid velocity (v_L) is only constrained by ensuring turbulent flow for proper mixing. In a system that resembles flow through a pipe, turbulent flow is achieved when the Reynolds number (*Re*) is above values of 3000–4000 (Acién Fernández et al., 2001; Carlozzi & Torzillo, 1996). By applying this condition, the minimum v_L can be then solved:

$$Re = \frac{\rho_L \cdot v_L \cdot d}{\mu_L} \geq 4000, \quad (1)$$

where ρ_L stands for the liquid density (kg m^{-3}) and μ_L the liquid dynamic viscosity (Pa s) of water at 37°C. This calculation results in a v_L of 0.05 m s^{-1}. Then, the corresponding *HRT* can be derived:

$$HRT = \frac{L}{v_L}. \quad (2)$$

Accordingly, the minimum v_L results in an *HRT* of 100 min for the long simulation. For the short simulation, we selected 0.20 m s^{-1} and hence a retention time of 25 min. This velocity lies at the lower limit of the range of velocities commonly employed in tubular photobioreactors operated autotrophically (Belohlav et al., 2021; Hall et al., 2003; Wongluang et al., 2013). Therefore, it can be considered at the upper limit of the desired velocities for *OBM*. Finally, for the medium simulation, we arbitrarily selected a retention time of 50 min, a value that falls in between the short and long retention times.

2.6 | Mixotrophic yield on substrate calculation

First, the total carbon (*TC*)-based amount of biomass produced in every batch was calculated (M_x, C-g). Because daily sampling did not match perfectly the volume increase due to glucose and base addition, the volume change was also taken into account:

$$M_x = C_x^f \cdot (V_{PBR} + \Delta V_{PBR}) \cdot C_{\%}^f - C_x^i \cdot V_{PBR} \cdot C_{\%}^i + \sum C_x^{sample} \cdot V_{sample} \cdot C_{\%}^{avg}, \quad (3)$$

where C_x^f and C_x^i are the biomass concentrations at the end and beginning of the batch, respectively (g L^{-1}). V_{PBR} is the working volume at the beginning of the batch (L) and ΔV_{PBR} is the net volume change at the end of the batch (L). $C_{\%}^f$ and $C_{\%}^i$ are the biomass carbon concentrations at the end and beginning of the batch (% w_C w_x^{-1}), respectively. In the last term, C_x^{sample} represents the biomass concentration of every monitoring sample (g L^{-1}), V_{sample} the volume of the sample, and $C_{\%}^{avg}$ the batch average biomass carbon concentration. Then, the *TC*-based amount of glucose consumed by the cells (M_s, C-g) was determined for every batch as follows:

$$M_s = \left(M_T \cdot C_g^{sol} - C_g^f \cdot (V_{PBR} + \Delta V_{PBR}) - \sum C_g^{sample} \cdot V_{sample}\right) \cdot C_{\%}^g, \quad (4)$$

where M_T (g) represents the total amount of 100 g L^{-1} glucose solution provided to the reactor and C_g^{sol} the glucose concentration in the glucose solution (g L^{-1}). C_g^f is the glucose concentration at the end of the batch (g L^{-1}) and C_g^{sample} is the glucose concentration of every sample (g L^{-1}). Finally, $C_{\%}^g$ indicates the carbon fraction of glucose (% w/w). The mixotrophic biomass yield on substrate ($Y^{mixo}_{x/s}$, C-g_x C-g_s^{-1}) was then derived for every batch:

$$Y_{x/s}^{mixo} = \frac{M_x}{M_s}. \quad (5)$$

2.7 | Assessment of contamination

Contamination was checked weekly during the experiments by DNA staining of culture samples with SYBR Green I (Sigma-Aldrich) and fluorescence microscopy with an EVOS FL auto microscope (Thermo Fisher Scientific). Presence of fluorescent bacterial or fungal cells is easily detectable by differences in size and shape compared to algal fluorescent cells.

2.8 | *PFD* measurements

PFD was measured with a Li-Cor 190-SA 2π quantum sensor (LI-COR Biosciences). Incident light intensity on the reactor surface was determined at 12 points inside the empty reactor vessel before every condition.

2.9 | Dry weight concentration

C_x was estimated by biomass dry weight (*DW*, g L^{-1}) determination in technical duplicates. Fresh aliquots of culture (1–5 mL) were diluted to 30 mL with demineralized water and filtered over preweighed Whatman GF/F glass microfiber filters (diameter of 55 mm, pore size 0.7 µm). The filters were washed with 30 mL of deionized water and dried at 100°C for at least 3 h.

2.10 | Average absorption cross-section

Average absorption cross section (a_x, m^2 kg_x^{-1}) in the photosynthetically active radiation region (400–700 nm) of the spectrum was determined as explained in detail in de Mooij et al. (2015). In short, fresh samples from the reactor were diluted to the range of 0.5–2 g L^{-1} *DW* and transferred to two cuvettes with an optical path of 2 mm. The absorbance was measured with a UV-VIS/double beam spectrophotometer (Shimadzu) equipped with an integrating sphere (ISR-2600).

2.11 | Photosystem II quantum yield (*QY*)

Fresh biomass samples were diluted to an optical density (*OD*) at 750 nm between 0.3 and 0.8 and incubated in darkness at 35°C for 20 min in duplicate. The dark-adapted photosystem II maximum *QY* of photochemistry (*QY*, F_v/F_m) was measured at 455 nm with an AquaPen-C AP-C 100 (Photon Systems Instruments).

2.12 | *TC* determination

Aliquots of culture were sampled at the end of every batch and centrifuged for 10 min at >20,000 relative centrifugal force (RCF). The supernatant was stored at −20°C. The pellets were washed twice with deionized water and stored at −20°C. Before measurement, both pellets and supernatants were thawed at room temperature and analyzed for *TC* ($g\ L^{-1}$) in duplicate with a TOC-L analyzer (Shimadzu). The biomass carbon content ($C_{\%}$, $\%w_C\ w_x^{-1}$) was calculated by dividing *TC* by the *DW* of the same sample.

2.13 | Coproporphyrin III (*COPROIII*) monitoring

Aliquots of culture were sampled from the reactor at different timepoints during all treatment batches and centrifuged for 10 min at >20,000 RCF. The supernatant was immediately used to measure *OD* at 400 nm in duplicate.

2.14 | *COPROIII* quantification

COPROIII identity and concentration were determined via an Agilent 1290 Infinity high performance liquid chromatography (HPLC) system (Agilent). The system consisted of a binary pump, an autosampler, an oven set at 25°C, and a fluorescence detector operated at 404 nm for excitation and 620 nm for emission. Aliquots of culture were sampled at the end of every batch and centrifuged for 10 min at >20,000 RCF. The supernatant was stored at −20°C. After thawing at room temperature, chromatographic separation of these liquid samples in duplicate was achieved on a Phenomenex Kinetex C18 RP 5 µm 4.6 × 150 mm (100 Å) column (Phenomenex). The flowrate was 1 mL min^{-1} and an injection volume of 20 µL was used. Total runtime was 14 min using a gradient of MilliQ water:acetonitrile:acetone (76:16:7.6) supplemented with 0.1% pyridine for peak sharpening and 0.1% phosphoric acid for acidification (Eluent A) and acetonitrile:methanol:acetone (60:30:10) (Eluent B). Eluent distribution was as follows: 0–5 min 0%–95% B, 5–7.5 min 95%–98% B, 7.5–9.5 min 98%–0% B, and 9.5–14 min 0% B. A calibration curve was made with *COPROIII* fluorescent standard (CFS-3 Frontier Specialty Chemicals) in a concentration range of 0.025–0.5 µg mL^{-1} diluted in 1 N HCl.

2.15 | Glucose quantification

Aliquots of culture were sampled from the reactor at different timepoints during all treatment batches and centrifuged for 10 min at >20,000 RCF. The supernatant was used to measure glucose concentration with a YSI 2950 Biochemistry Analyzer (YSI Life Sciences).

2.16 | Organic acids, alcohols, and trehalose quantification

Aliquots of culture were sampled at the end of every batch and centrifuged for 10 min at >20,000 RCF. The supernatant was stored at −20°C. After thawing at room temperature, the liquid samples were analyzed in duplicate with respect to ethanol, glycerol, citric acid, lactic acid, acetic acid, succinic acid, pyruvic acid, formic acid, and trehalose using an Agilent 1290 Infinity HPLC system (Agilent), with an Agilent 1290 Infinity Binary Pump, Agilent 1290 Infinity Autosampler, Agilent 1290 Infinity diode array detector operated at 210 nm and an Agilent 1260 Infinity RI detector operated at 45°C. The HPLC was operated with a Rezex ROA-Organic Acid H + 300 × 7.8 mm (Phenomenex) column and a SecurityGuard guard column Carbo-H-4 × 3.0 mm (Phenomenex) at 60°C and 0.008 mM H_2SO_4 as mobile phase at 0.8 mL min^{-1} as flow rate.

2.17 | Carbohydrates quantification

Carbohydrates in the supernatant were determined by the colorimetric method proposed by Dubois et al. (1956). Aliquots of culture were sampled at the end of every batch and centrifuged for 10 min at >20,000 RCF. The supernatant was stored at −20°C. Before the analysis, samples were thawed at room temperature. 50 µL of the sample and 450 µL of medium were added to glass tubes in duplicate. Then, 500 µL of 5% w/w phenol solution were added to the tubes and subsequently 2.5 mL of concentrated sulfuric acid were also added without active mixing. The samples were incubated first at room temperature for 10 min and then at 35°C for 30 min. During the latter samples were vortexed every 5 min. After the incubation, absorbance was measured at 483 nm. Glucose was used as a reference for the standard curve in a range of 0–0.1 $g\ L^{-1}$.

2.18 | Soluble protein quantification

Aliquots of culture were sampled at the end of every batch and centrifuged for 10 min at >20,000 RCF. The supernatant was stored at −20°C and thawed at room temperature when used for analysis. Soluble protein concentration in the supernatant was determined in duplicate with the DC Protein Assay kit from Bio-Rad, following the principle of Lowry's method. Absorbance was determined at 750 nm and bovine serum albumin was used as standard in a range of 0 – 1.4 $mg\ L^{-1}$.

2.19 | Statistical procedures

Propagation of errors for addition operations was calculated according to Equation (6):

$$\sigma_z = \sqrt{\sigma_x^2 + \sigma_y^2 + \ldots}, \tag{6}$$

Propagation of errors for multiplication operations was calculated according to Equation (7):

$$\frac{\sigma_z}{z} = \sqrt{\frac{\sigma_x^2}{x} + \frac{\sigma_y^2}{y} + \ldots}. \tag{7}$$

where σ_x is the standard deviation associated with the value x and so on.

3 | RESULTS AND DISCUSSION

3.1 | Determination of pulse length

In this work, three different experimental conditions were tested in three respective experiments: long, medium, and short tube retention time simulation of a tubular reactor operated under nonaerated mixotrophy. Each condition aimed to study the effect of glucose and oxygen fluctuations in a lab-scale reactor by feeding glucose in pulses of different lengths. Pulse length was manually adjusted at the beginning of every experimental condition to match the aimed periods of 100, 50, and 25 min between each pulse, as it is explained in detail in Section 2.

The system was instable and showed variability in cycle length, even when keeping pumping time constant. Moreover, increases or decreases in pumping time did not result in proportional increases or decreases in cycle length. Therefore, after some initial adjustments, we selected pumping times of 172, 47, and 19 s for the long, medium, and short condition, respectively. These pumping times generated time periods between every *DO* peak of 112 ± 36, 71 ± 24, and 21 ± 4 min at the beginning of the second batch. Even if they deviated from the desired periods, they were selected as they were giving close-to-stable cycles and thus were maintained during the following batches of each condition. The resulting experimental *DO* profiles are displayed in Figure 2.

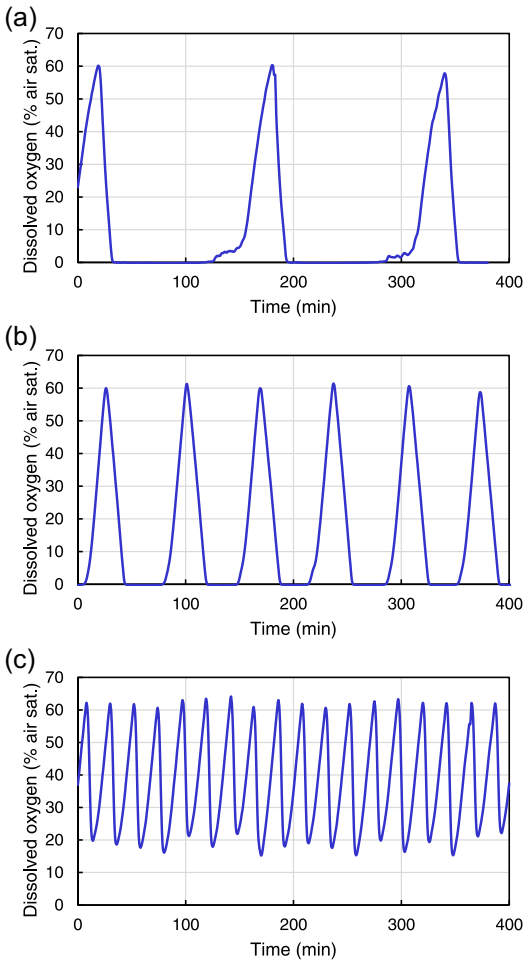

FIGURE 2 Experimental stable dissolved oxygen concentration patterns obtained in the long (a), medium (b), and short (c) conditions after the initial adjustments.

3.2 | *COPROIII* accumulated in the medium

During the long and medium tube retention time simulations, *DO* decreased from 60% to 0% air saturation between consecutive *DO* peaks, while in the short tube retention time simulation, it always remained above 10%. This means that during the long and medium conditions, the cells experienced cyclic periods of anoxia (Figure 2). These periods were not purely anaerobic, as photosynthesis was still happening but oxygen demand surpassed oxygen production. In fact, *DO* increased immediately when glucose was depleted. We monitored anoxic stress in the cultures by indirectly measuring the accumulation of *COPROIII* in the supernatant, displayed in Figure 3. This molecule has been previously identified as a marker of anoxia in *G. sulphuraria* (Sarian et al., 2016; Zhu et al., 2022). Because it is released to the supernatant and has a characteristic pink color, it can be easily detected by measuring absorbance with a spectrophotometer at 400 nm. In addition, we confirmed the identity of the molecule by HPLC and excluded the possibility of having a mixture of porphyrins with similar absorbance properties (Supporting Information: Figure S1). *COPROIII* accumulated during every batch of the long and medium conditions, while it barely changed in the short one where oxygen never reached 0 (Figure 3). These results indicate that cells endured oxygen limitation during the long and medium conditions, even if photosynthetic oxygen production was still ongoing. Moreover, the results add more evidence supporting that *COPROIII* excretion is indeed caused by oxygen limitation and not by the presence of glucose (Stadnichuk et al., 1998) or as a wavelength-shifting mechanism (Ternes, 2015).

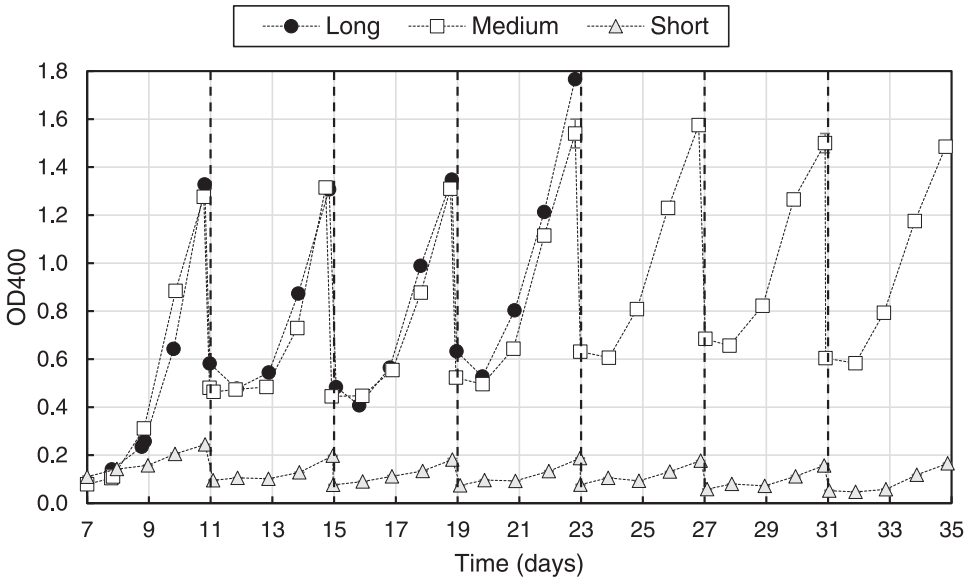

FIGURE 3 Coproporphyrin III accumulation measured as absorbance of the supernatant at 400 nm during the long (circles, black), medium (squares, white), and short (triangles, gray) tube retention time simulations from the second batch onward. Dashed lines indicate the duration of the batches. Values expressed as averages ± standard deviation.

COPROIII results from the spontaneous oxidation of *COPROGEN*, an intermediary in the synthesis pathway of chlorophyll, phycobilin, and the group heme (Hansson & Hederstedt, 1994). Under aerobic conditions, *COPROGEN* is oxidized to protoporphyrinogen IX by HemF. This enzyme has been putatively identified as Gasu_19740 in the genome of *G. sulphuraria*, which also contains a putative isoform, Gasu_14610 (Caspi et al., 2014). Under the two conditions tested in this study in which oxygen was cyclically limiting, we observed a remarkable increase of *COPROIII* in the supernatant of the cultures. In these two scenarios, the activity of HemF might have not proceeded at normal rate due to the lack of oxygen or its expression might have been downregulated (Goto et al., 2010; Kim et al., 2015). Consequently, *COPROGEN* accumulated in the cell and was either released and oxidized to *COPROIII* extracellularly or oxidized in the cell and released as *COPROIII*. Its excretion, possibly at the expense of energy (Krishnamurthy et al., 2007), might be beneficial as the light activity of the tetrapyrrole ring might be a source of damaging ROS within the cell (Sułek et al., 2020).

Interestingly, the genome of *G. sulphuraria* also contains a putative HemN (Gasu_49660), an oxygen-independent enzyme that catalyzes the conversion of *COPROGEN* to protoporphyrinogen IX employing S-adenosyl methionine (Caspi et al., 2014). However, if active, HemN could not completely compensate for the loss of activity of HemF in our study. The residual presence of oxygen might have been enough to interfere with the oxygen-sensitive [4Fe-4S] cluster of the enzyme or perhaps prevent its activation. This result is line with the study of Sarian et al. (2016). In that work, *G. sulphuraria* was cultivated mixotrophically without aeration and the oxygen remained at 0% air saturation for days. Similarly to our study, the cultures were photosynthetically active and, therefore, there was oxygen production inside the cells, which might have also interfered with the activation of HemN.

3.3 | Oxygen limitation resulted in reduced pigment content

The average absorption cross section (a_x, $m^2 kg_x^{-1}$) was measured daily over the course of the experiments to keep track of pigment levels in the cells (Figure 4). At the beginning of the second batch, a_x had reached values in the range of 150–180 $m^2 kg^{-1}$ under all three conditions. After this batch, a_x had a pronounced decrease in the medium and long tube retention time simulations, going down to 50–70 $m^2 kg_x^{-1}$ from batch 3 onward. In the short tube retention time simulation, a_x also experienced a reduction, but to a considerably lower extent, stabilizing in the range of 130–140 $m^2 kg_x^{-1}$ at the end of batches 3–8.

These results match the previously discussed observations of *COPROIII* accumulation. In the medium and long tube retention time simulations in which oxygen was periodically depleted, *COPROIII* accumulated in the supernatant and a_x had a twofold reduction compared to the short tube retention time simulation. The lack of oxygen in these two conditions impaired pigment synthesis at least at the level of coproporphyrinogen III (*COPROGEN*) oxidation, which led to a nonregulatory reduction of the antenna of *G. sulphuraria*. This effect was absent in the short condition, in which *DO* remained always above 10% air saturation and no signs of oxygen limitation were observed. An additional explanation for these differences in a_x could also come from different light exposures and, therefore, acclimation to different illumination levels. However, the light intensity and biomass concentration range were the same in the three conditions. In other words, the specific light supply experienced by the cells was similar, and therefore, their pigment content should have adapted similarly. As this was not the case, we can conclude that the

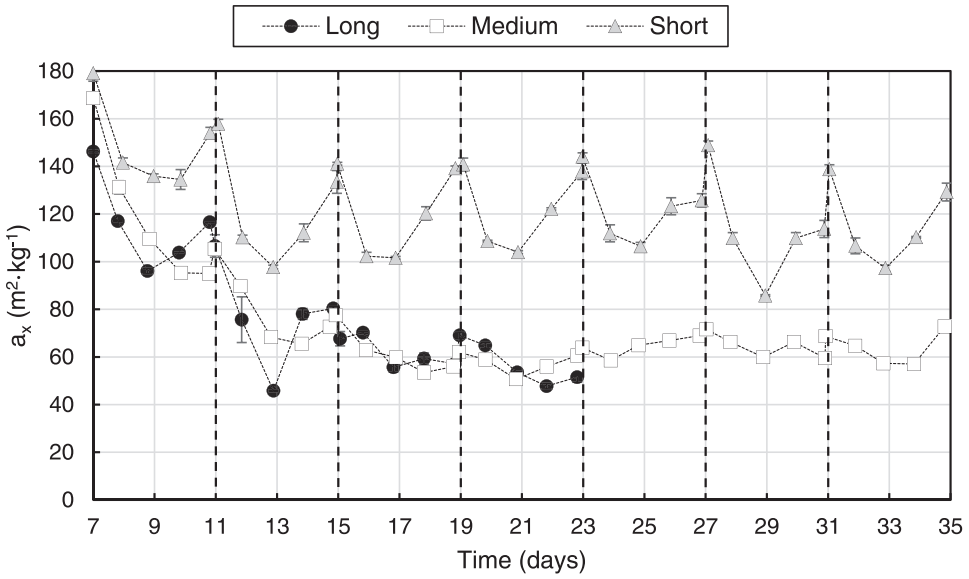

FIGURE 4 Average absorption cross section (a_x, $m^2\ kg^{-1}$) during the long (circles, black), medium (squares, white), and short (triangles, gray) tube retention time simulations from the second batch onward. Dashed lines indicate the duration of the batches. Values expressed as averages ± standard deviation.

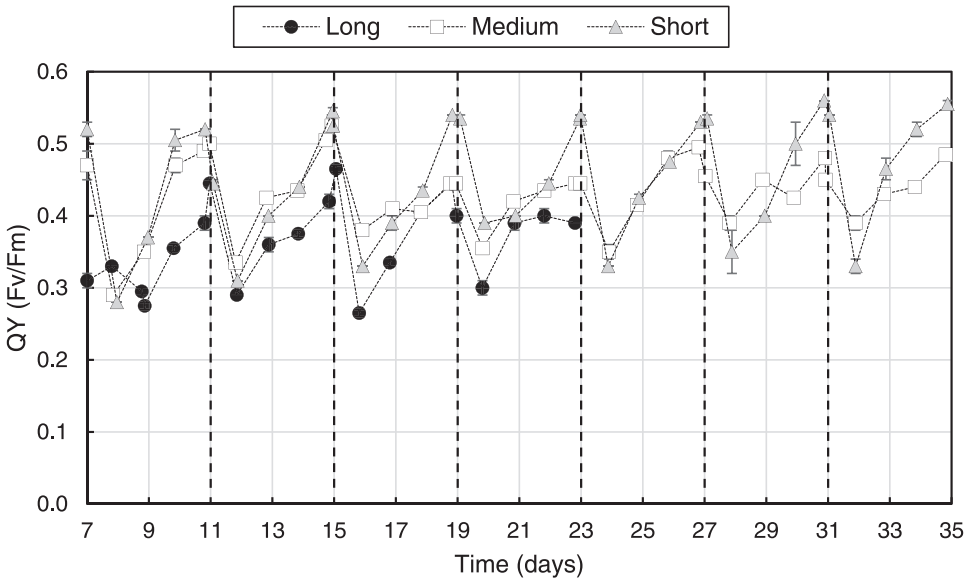

FIGURE 5 Photosystem II dark-adapted quantum yield (QY, *Fv/Fm*) during the long (circles, black), medium (squares, white) and short (triangles, gray) tube retention time simulations from the second batch onward. Dashed lines indicate the duration of the batches. Values expressed as averages ± standard deviation.

differences arose due to oxygen limitation in two of the three conditions.

In parallel to the a_x, we also monitored the *QY* of the cultures during the study (Figure 5). After every dilution, *QY* first dropped and then started recovering after the second day of the batches, reaching maximum values by their end. Interestingly, no considerable differences were observed in the *QY* maxima between the three conditions despite the divergence in a_x trends. Nevertheless, the highest values were still obtained in the short tube retention time simulation, where *QY* remained always above 0.50 at the end of the batches. This is an indication that the reduction in pigment content might have not had a direct impact in the electron transfer of the photosynthetic apparatus, or at least not significantly in the conditions tested.

When considering the implementation of this process in a real tubular photoreactor, it is relevant to look at the time frame of the effects here described. In the medium tube retention time

condition, a_x decreased steeply in the second and third batch, staying at similar levels until the eighth batch. In the long tube retention time condition, a_x also decreased mainly until the third batch, staying stable from that point onward. Unfortunately, due to a technical problem, this run stopped after the fifth batch. After the steep decrease of the first batches in the medium and long tube retention time simulations, we expected that a_x would decrease progressively until the culture crashed. Nevertheless, after reaching 50 $m^2\,kg^{-1}$, a_x did not decrease further and we also did not observe a pronounced decrease in *QY*. Due to time limitations, we stopped the medium condition after the eighth batch had finished. The apparent equilibrium situation might represent the threshold pigment content that the residual activity of HemF and the activity HemN are able to sustain. Even if the cultures did not immediately crash, it remains unclear whether cell viability would be sustainable in the long term under these conditions. For example, under changing outdoor light irradiance, algal cells require flexibility adjusting their antenna. Furthermore, limited pigment synthesis is not a suitable strategy to accumulate the main product of *G. sulphuraria*, C-phycocyanin. *COPROGEN* is also a precursor in the synthesis of the chromophore group of this phycobiliprotein, phycocyanobilin (Mulders et al., 2014).

Despite the continuous presence of oxygen in the medium, in the short tube retention time simulation, there was still a slight antenna reduction from the first batch to the second. In this case, the reduction can be explained by acclimation to the illumination profile in the reactor. We have previously observed that when shifting from autotrophy to mixotrophy, *G. sulphuraria* experiences a reduction in a_x. In a previous study with the same reactor setup, a_x at the end of a mixotrophic repeated batch experiment also lay in the range of 130–140 $m^2\,kg^{-1}$ (Abiusi et al., 2021). Interestingly, in that study, *DO* was maintained stable at 90% air saturation throughout the whole reactor run, suggesting that the oxygen disturbances of the short condition had no noticeable effect on the pigment content. This adaptation also happened in the long and medium conditions, however, the drastic effect of the anoxic cycles covered the small reduction caused by adaptation to mixotrophy.

3.4 | Substrate utilization

Besides oxygen availability, the other important factor to compare among the different conditions tested in this study is the efficiency of substrate utilization. In this section, the focus is given to the mixotrophic yield on substrate ($Y^{mixo}_{x/s}$, C-g C-g^{-1}), whereas productivities and growth rates are not discussed. We centered our analysis in this parameter because maximizing the degree of substrate conversion is one of the goals in *OBM*. Furthermore, the three experimental conditions tested in this study, which we have called long, medium, and short tube retention times, were obtained providing glucose pulses of different lengths. As the control system was based on *DO* levels, the number of pulses was not fixed and varied between batches and conditions. Because of this, the total amount of glucose provided to the reactor is not exactly the same from batch to batch and from condition to condition. For this reason, the mixotrophic productivities of the three runs are not directly comparable. To take into account the different amounts of glucose supplied, we can better compare substrate utilization by looking at $Y^{mixo}_{x/s}$. $Y^{mixo}_{x/s}$ at the end of every batch is reported in Table 1.

We obtained yields ranging between 0.70 and 0.86 C-g C-g^{-1}, with most of the batches laying within the range of 0.75–0.82. No clear upward or downward trend can be determined throughout any of the experiments, as higher and lower results are obtained regardless of time progression. These values suppose a reduction of 4%–22% of the yields accomplished in previous studies with *OBM*. For example, 0.92 and 0.89 C-g C-g^{-1} have been achieved in repeated batch (Abiusi et al., 2021) and in chemostat modes with *G. sulphuraria* ACUF 064, respectively (Abiusi et al., 2022). In the former publication, it was observed that mixotrophic metabolism requires a period of adaptation (i.e., several batches) to reach high yields on the substrate. Nevertheless, in that case, 0.92 C-g C-g^{-1} was obtained already in the third batch, while in this study, such value could not be reached even after seven batches.

Changes in biomass composition, maybe triggered by the conditions of this study, could affect the maximum theoretical yield of *OBM* as it is determined stoichiometrically (Abiusi et al., 2020a).

TABLE 1 Measured and recalculated mixotrophic biomass yield on substrate ($Y^{mixo}_{x/s}$, C-g·C-g^{-1}) at the end of every batch from the long, medium and short tube retention time simulations.

Batch	2	3	4	5	6	7	8
Measured							
Long	0.80 ± 0.03	0.80 ± 0.01	0.76 ± 0.02	0.84 ± 0.12	-	-	-
Medium	0.82 ± 0.03	0.70 ± 0.01	0.80 ± 0.01	0.82 ± 0.01	0.86 ± 0.04	0.81 ± 0.05	0.79 ± 0.03
Short	0.79 ± 0.03	0.77 ± 0.04	0.77 ± 0.03	0.79 ± 0.03	0.76 ± 0.02	0.75 ± 0.05	0.80 ± 0.02
Recalculated							
Long	0.88 ± 0.04	0.89 ± 0.03	0.84 ± 0.02	0.96 ± 0.12	-	-	-
Medium	0.87 ± 0.03	0.78 ± 0.03	0.86 ± 0.01	0.88 ± 0.01	0.94 ± 0.04	0.88 ± 0.05	0.85 ± 0.03
Short	0.85 ± 0.03	0.83 ± 0.04	0.84 ± 0.03	0.87 ± 0.03	0.83 ± 0.02	0.82 ± 0.05	0.86 ± 0.02

Note: The recalculated $Y^{mixo}_{x/s}$ resulted from adding the excreted carbon to the carbon in the biomass. Values expressed as averages ± standard deviation.

However, considerable changes in biomass composition are unlikely and even if present, cannot explain by themselves a decrease as pronounced as 22%. A decrease in yield might also indicate carbon redirection toward a certain product, such as the aforesaid *COPROIII*. From a broader perspective, a reduction in carbon utilization efficiency is a common phenomenon in the scale-up of aerobic heterotrophic processes (Lara et al., 2006). Substrate and oxygen fluctuations are usually behind of this unwanted effect, as they might trigger overflow metabolic responses, transient activation of the fermentation pathways, increased maintenance requirements, or other stress responses (Nadal-Rey et al., 2021). In the dynamic environment of our scale-down study, cells underwent glucose feast and famine, as well as sufficient oxygen availability and scarcity or even complete depletion. Correspondingly, one of the first things to determine to fill in the carbon gap is the presence and quantity of excretion products in the medium.

3.5 | Carbon was excreted to the supernatant

In search of the missing carbon, we looked for any excretion by measuring *TC* in the supernatant of the cultures at the end of every batch. Strikingly, our measurements found 0.28–0.57 g L^{-1} of carbon in the supernatant depending on the batch (Table 2, Raw TC). The medium employed in the experiments does not contain any source of carbon apart from EDTA, present at a concentration of 100 C-mg L^{-1}. We assumed that EDTA stayed stable throughout the experiments and that the cells did not degrade it. In addition, we monitored glucose concentration along the experiments, including the concentration at the end of the batches (Table 2, Glucose). Accordingly, by subtracting the carbon present in EDTA and glucose from the *TC* measurements, we can determine the amount of carbon resulting from biological activity. Overall, with this correction, we obtained concentrations between 0.16 and 0.42 C-g L^{-1} (Table 2, Corrected TC). In Table 1, we recalculated $Y^{mixo}_{x/s}$ by adding the carbon present in the supernatant as if it were part of the biomass. The addition of excreted carbon to the biomass would result in yields ranging from 0.78 to 0.96 C-g C-g^{-1}, with all batches but one obtaining results ≥0.82. With this increase, the recalculated values are either similar or closer to the maximum $Y^{mixo}_{x/s}$ obtained in previous studies (Abiusi et al., 2021, 2022), closing the carbon gap. However, despite the recalculation, there is still some deviation among the results. This might be a result of the combined effects of the inherent variability of batch processes and the large deviation obtained in some of the *TC* measurements.

We cannot completely exclude that $Y^{mixo}_{x/s}$ could have also been partially affected by increased cellular maintenance requirements, and thus, a higher fraction of carbon lost as CO_2. In fact, this phenomenon has already been noticed in *G. sulphuraria* (Graverholt & Eriksen, 2007). In our study, oxygen and glucose changes were in the order of tens of minutes, sufficient for continuous cycles of regulation at the protein level. These would have resulted in increased energy demand, consequently channeling more substrate into energy production. In principle, during our mixotrophic process, the autotrophic metabolism is also active and recycling the CO_2 from respiration back into biomass. However, momentary peaks of CO_2 production might have overloaded the carbon fixing capacity, perhaps also affected by the pigment disruption caused by oxygen limitation. Regrettably, this could not be validated due to the lack of active aeration during *OBM*. Gas production derived from algal metabolism by itself was too low to be detected by our gas analyzer. Nonetheless, based on the *TC* measurements, we can still conclude that the decrease in $Y^{mixo}_{x/s}$ was mainly caused by carbon leakage into the supernatant.

3.6 | Cells produced extracellular carbohydrates and proteins

When looking at the possible causes that explain the presence of carbon in the supernatant, the first suspect is the accumulation of *COPROIII* in the medium, described in previous sections. This hypothesis was ruled out by measuring the concentration of *COPROIII* with HPLC at the end of every batch. The results of this analysis are shown on Table 2. In the long and medium tube retention time conditions, where *COPROIII* showed a significant accumulation, the amount of this component released to the medium was close to 1 mg L^{-1}. On the other hand, in the short condition, *COPROIII* presence was 10 times lower, with concentrations in the order of 0.1 mg L^{-1}. These are, respectively, three and four orders of magnitude lower than the carbon found in the supernatant, and thus have a negligible effect on the final $Y^{mixo}_{x/s}$. The fact that *COPROIII* was not the main cause of carbon loss agrees with the results of the short condition. In this simulation, $Y^{mixo}_{x/s}$ was similar to the long and medium conditions while no clear *COPROIII* accumulation was observed.

An alternative explanation for the decrease in $Y^{mixo}_{x/s}$ might come from the aforementioned excretion of fermentation products triggered by glucose and oxygen fluctuations. To validate this hypothesis, we scrutinized the supernatant of the experiments by means of HPLC. In total, we monitored citric acid, lactic acid, acetic acid, succinic acid, pyruvic acid, formic acid, trehalose, ethanol, and glycerol. None of these compounds were detected in the supernatant. In a prior study with heterotrophic cultures of *G. sulphuraria*, the algal cells were subject of similar cycles of glucose availability and depletion (Graverholt & Eriksen, 2007). The authors did not detect any excreted molecule as a result. The maximum glucose concentration reached in that study was 0.5 g L^{-1}, while in our work it was 0.6, 0.2, and 0.1 g L^{-1} for the long, medium, and short conditions, respectively (data not shown). As maximum concentrations were in the same range, this is an additional indication to dismiss the fermentation pathway transient activation hypothesis.

Interestingly, the carbon excretion was identified as a mixture of carbohydrates and proteins by means of the Dubois and Lowry methods (Table 2). Carbohydrates were estimated in the order of

TABLE 2 Raw total carbon (*Raw TC*, C-g L^{-1}), glucose (mg L^{-1}), corrected total carbon (*Corrected TC*, C-g L^{-1}), coproporphyrin III (*COPROIII*, mg L^{-1}), carbohydrates (g L^{-1}), proteins (g L^{-1}) and calculated carbon content in the extracellular polymeric substance (*EPS TC*, C-g L^{-1}) measured in the supernatant at the end of every batch from the long, medium and short tube retention time simulations.

Batch	2	3	4	5	6	7	8
Raw TC							
Long	0.57 ± 0.11	0.53 ± 0.12	0.38 ± 0.03	0.54 ± 0.02	-	-	-
Medium	0.28 ± 0.01	0.36 ± 0.08	0.31 ± 0.01	0.32 ± 0.00	0.38 ± 0.01	0.35 ± 0.00	0.32 ± 0.00
Short	0.32 ± 0.01	0.33 ± 0.02	0.35 ± 0.02	0.37 ± 0.02	0.34 ± 0.01	0.32 ± 0.00	0.33 ± 0.01
Glucose							
Long	194.3 ± 1.3	13.5 ± 0.5	56.3 ± 11.7	129.8 ± 5.2	-	-	-
Medium	63.2 ± 4.5	44.3 ± 1.3	75.3 ± 5.3	63.7 ± 1.3	43.5 ± 2.5	37.3 ± 0.7	46.5 ± 2.2
Short	47.5 ± 1.5	49.2 ± 1.2	53.7 ± 4.3	44.2 ± 5.2	47.5 ± 1.8	53.2 ± 0.8	58.8 ± 1.2
Corrected TC							
Long	0.39 ± 0.11	0.42 ± 0.12	0.25 ± 0.03	0.39 ± 0.02	-	-	-
Medium	0.16 ± 0.01	0.24 ± 0.08	0.18 ± 0.01	0.20 ± 0.00	0.26 ± 0.01	0.23 ± 0.00	0.21 ± 0.00
Short	0.20 ± 0.01	0.21 ± 0.02	0.23 ± 0.02	0.25 ± 0.02	0.22 ± 0.01	0.20 ± 0.00	0.20 ± 0.01
COPROIII							
Long	1.49 ± 0.09	1.39 ± 0.04	1.50 ± 0.03	1.74 ± 0.24	-	-	-
Medium	1.60 ± 0.08	1.26 ± 0.07	1.49 ± 0.01	1.79 ± 0.06	1.72 ± 0.11	2.16 ± 0.00	2.11 ± 0.00
Short	0.18 ± 0.01	0.15 ± 0.01	0.13 ± 0.00	0.14 ± 0.00	0.14 ± 0.00	0.13 ± 0.00	0.14 ± 0.00
Carbohydrates							
Long	0.42 ± 0.00	0.43 ± 0.02	0.29 ± 0.00	0.49 ± 0.02	-	-	-
Medium	0.28 ± 0.03	0.28 ± 0.02	0.30 ± 0.01	0.33 ± 0.01	0.27 ± 0.05	0.36 ± 0.02	0.39 ± 0.03
Short	0.25 ± 0.01	0.34 ± 0.01	0.30 ± 0.01	0.35 ± 0.02	0.31 ± 0.01	0.26 ± 0.04	0.32 ± 0.01
Proteins							
Long	0.20 ± 0.01	0.21 ± 0.00	0.15 ± 0.03	0.17 ± 0.00	-	-	-
Medium	0.14 ± 0.03	0.16 ± 0.01	0.21 ± 0.01	0.17 ± 0.01	0.24 ± 0.02	0.21 ± 0.00	0.17 ± 0.01
Short	0.17 ± 0.03	0.17 ± 0.01	0.22 ± 0.03	0.21 ± 0.03	0.17 ± 0.03	0.14 ± 0.00	0.22 ± 0.00
EPS TC							
Long	0.27 ± 0.00	0.29 ± 0.01	0.19 ± 0.01	0.29 ± 0.01	-	-	-
Medium	0.19 ± 0.02	0.20 ± 0.01	0.23 ± 0.01	0.22 ± 0.00	0.23 ± 0.02	0.26 ± 0.01	0.24 ± 0.01
Short	0.19 ± 0.02	0.23 ± 0.01	0.24 ± 0.01	0.25 ± 0.02	0.21 ± 0.02	0.18 ± 0.02	0.24 ± 0.00

Note: Values expressed as averages ± standard deviation.

0.25–0.49 g L^{-1}, with the highest values corresponding to the long tube retention time simulation, as only in this run concentrations surpassed 0.40 g L^{-1}. On the other hand, protein concentration was in the range of 0.14–0.24 g L^{-1}, with no clear differences among conditions. These results are in agreement with the pattern of *TC* measurements, as higher values were also found for the long condition. The combination of carbohydrates and proteins, with a larger fraction of the former, suggests that the cells were producing extracellular polymeric substances (*EPSs*). *EPSs* are common and have been extensively studied in some species of cyanobacteria and microalgae, including red microalgae such as *Porphyridium purpureum* (Cruz et al., 2020; Pierre et al., 2019). Despite having a rigid cell wall, *G. sulphuraria* has been reported to retain the ability to form an extracellular mucilage matrix, although possibly at very low amounts and not always (Gaignard et al., 2019; Lang et al., 2020; Oesterhelt et al., 2008; Vis & Necchi, 2021; Weber et al., 2007). In fact, *EPSs* have been only recently measured in this species and their functions have not been investigated yet (Sun et al., 2021; Zhu et al., 2022). In other photosynthetic microorganisms, *EPSs* serve a plethora of functions, including providing structural support, external nutrient storage, or protection against environmental stresses (Flemming & Wingender, 2010).

We did not observe more biofilm formation (data not shown) than former studies with the same strain in the same system (Abiusi et al., 2022). Additionally, no special treatment had to be performed to separate the *EPS* from cells rather than a simple centrifugation step, indicating that the produced *EPS* are released rather than cell-bound. This suggests that the *EPS* had a nonstructural function under the conditions tested in this study. Zhu et al. observed both porphyrin and *EPS* accumulation in the supernatant of a mixotrophic *G. sulphuraria* culture (Zhu et al., 2022). During their experiment, *DO* remained below 10% for days at certain periods, indicating a possible oxygen limitation with similar effects to the anoxic cycles of our study. Under these conditions of oxygen limitation, *EPS* production might have been triggered to serve as an electron sink contributing to the cell redox balance by recycling reduced cofactors when oxygen was not available (Pereira et al., 2022). However, in principle, this hypothesis cannot explain *EPS* production in our short condition, as *DO* remained always above 10% air saturation. Another explanation could be that the carbon excreted in the form of *EPS* constitutes an extracellular carbon reservoir that is readily available to be reuptaken whenever certain conditions are met. Similar phenomena have been observed in cyanobacteria and diatoms (Miyatake et al., 2014; Stuart et al., 2016). An external carbon and energy storage might help *G. sulphuraria* to endure periods of light scarcity, frequent in the environments that they colonize (Gross & Oesterhelt, 1999). In the dynamic environment of our scale-down study, cells underwent cycles of glucose feast and famine which could have triggered a nutrient storing response. Perhaps, rather than a monocausal origin, it is the combined the effect of glucose and oxygen fluctuations what triggers production of *EPS*. Further insight into *EPS* production in *G. sulphuraria* is required to establish their specific function in this context.

Assuming an average carbon content of 44% for the carbohydrates and 53% for the proteins (Rouwenhorst et al., 1991), we can estimate carbon excreted in the form of these two macromolecules by simple addition. The results of the calculation are in the range of 0.18–0.29 C-g L^{-1} (Table 2, *EPS TC*). The carbon amount calculated in this manner matches to a considerable extent the corrected *TC* measurements for all three conditions. The small remaining discrepancies are probably caused by two factors. First, the aforementioned large technical deviation in some of the raw *TC* measurements. This might have led to the overestimation of some values, especially in the samples of the long condition. Second, it is important to remark that for the Lowry and Dubois measurements, we used glucose and bovine serum albumin as standards, respectively. These standards might just offer an approximation, as the composition of the *EPS* is unknown. In conclusion, the carbon balance indicates that the excreted carbon was indeed mainly part of either carbohydrates or proteins.

3.7 | Scale-up implications and limitations of the current study

Herewith, we intended to reproduce the oxygen and glucose profiles of a tubular photobioreactor operated under *OBM* in a lab-scale system. By studying cell behavior under these conditions, we wanted to understand how the scale-up might affect cell physiology and prevent detrimental effects in the future. The results pointed at two clear, interesting consequences of scale-up: (1) pigment synthesis disruption and (2) lowered efficiency of substrate utilization. Both outcomes affect the process negatively, and as such, must be taken into account when planning the actual *OBM* scale-up to the extent possible. Concerning (1), special attention should be placed on keeping *DO* concentrations above limiting levels. This implies that a simplistic and straightforward adaptation of our current lab-scale *DO* control strategy, explained elsewhere (Abiusi et al., 2020a), might not be sufficient to achieve so. In the case of (2), carbon excretion is most likely triggered by glucose and oxygen fluctuations. In practice, this suggests that glucose and oxygen profiles within the reactor have to be kept as flat as possible. Hence, glucose feeding has to be tightly regulated and the control strategy should be fast enough to react to small changes in oxygen concentration.

No scale-down study is perfect, and thus it is important to acknowledge its constraints. Due to technical limitations in the automation of our setup, the employed pulse glucose feeding strategy was only implemented with constant and continuous illumination during the experiments. When scaling up the process outdoors, however, the microalgae will deal with day/night cycles. During nighttime, there will not be photosynthetic oxygen production and therefore fresh air will need to be provided to compensate for respiration. The repercussion of nightly aeration and of day/night cycles per se in the mechanisms described here is uncertain. For instance, periodic aeration during the night could reduce the extent of the oxygen limitation experienced by the cells and consequently diminish *COPROIII* accumulation. Additionally, the metabolic response of synchronized cells to glucose and oxygen fluctuations might differ from what was observed here, for example, in terms of carbon excretion. Although our study offers valuable information as first approximation to the matter, the described limitations must be considered in the following steps of the scale-up design.

4 | CONCLUSION

Glucose supply in pulses created fluctuations of glucose and *DO* in our lab-scale reactor resembling those expected in a tubular photobioreactor operated under *OBM*. Pulse length was adjusted to represent long, medium, and short tube retention times. In the long and medium conditions, *DO* was cyclically depleted. As a consequence, the chlorophyll synthesis pathway of *G. sulphuraria* was disrupted and *COPROIII* accumulated in the supernatant. Moreover, the absorption cross-section of the cells was drastically reduced from 150–180 to 50–70 $m^2\,kg^{-1}$. In the three conditions, we obtained biomass yields on substrate in the range of 0.70–0.86, a 22%–4% reduction of the maximum yields obtained previously with this process. The missing carbon was found in the supernatant in the form of carbohydrates and proteins, a form of *EPS* possibly with a nonstructural function. The results highlight the importance of designing a tightly controlled glucose supply in the following steps

of the scale-up. The scale-down approach, not deprived of limitations, is a powerful tool to derisk the scale-up process of newly developed cultivation systems such as *OBM*.

AUTHOR CONTRIBUTIONS

Pedro Moñino Fernández: Conceptualization, methodology, investigation, formal analysis, data curation, writing-original draft, writing review and editing, visualization. **Albert Vidal García**: Investigation, formal analysis. **Tanisha Jansen**: Investigation, formal analysis. **Wendy Evers**: Methodology, investigation. **Maria Barbosa**: Supervision, writing review and editing, funding acquisition. **Marcel Janssen**: Conceptualization, supervision, writing review and editing.

ACKNOWLEDGMENTS

The authors thank Sander Roessink, Cathrien Diepenhorst-Wieland and the Klinisch Chemisch Laboratorium from the Deventer Hospital for providing and assisting in the adaptation of their method for HPLC coproporphyrin III quantification. This work was supported by ProFuture project (2019–2023) "Microalgae protein-rich ingredients for the food and feed of the future"-H2020 Ref. 862980.

CONFLICT OF INTEREST STATEMENT

The authors declare no conflict of interest.

DATA AVAILABILITY STATEMENT

The data that support the findings of this study are available from the corresponding author upon reasonable request.

ORCID

Pedro Moñino Fernández http://orcid.org/0000-0002-0311-1246
Albert Vidal García https://orcid.org/0000-0001-8290-916X
Tanisha Jansen https://orcid.org/0000-0001-6615-2064
Marcel Janssen https://orcid.org/0000-0002-5754-6050

REFERENCES

Abiusi, F., Moñino Fernández, P., Canziani, S., Janssen, M., Wijffels, R. H., & Barbosa, M. (2022). Mixotrophic cultivation of *Galdieria sulphuraria* for C-phycocyanin and protein production. *Algal Research*, *61*, 102603. https://doi.org/10.1016/j.algal.2021.102603

Abiusi, F., Trompetter, E., Hoenink, H., Wijffels, R. H., & Janssen, M. (2021). Autotrophic and mixotrophic biomass production of the acidophilic *Galdieria sulphuraria* ACUF 64. *Algal Research*, *60*, 102513. https://doi.org/10.1016/j.algal.2021.102513

Abiusi, F., Wijffels, R. H., & Janssen, M. (2020a). Doubling of microalgae productivity by oxygen balanced mixotrophy. *ACS Sustainable Chemistry & Engineering*, *8*(15), 6065–6074. https://doi.org/10.1021/acssuschemeng.0c00990

Abiusi, F., Wijffels, R. H, & Janssen, M. (2020b). Oxygen balanced mixotrophy under day-night cycles. *ACS Sustainable Chemistry & Engineering*, *13*, 34. https://doi.org/10.1021/acssuschemeng.0c03216

Acién Fernández, F. G., Fernández Sevilla, J. M., Sánchez Pérez, J. A., Molina Grima, E., & Chisti, Y. (2001). Airlift-driven external-loop tubular photobioreactors for outdoor production of microalgae: Assessment of design and performance. *Chemical Engineering Science*, *56*(8), 2721–2732. https://doi.org/10.1016/S0009-2509(00)00521-2

Belohlav, V., Uggetti, E., García, J., Jirout, T., Kratky, L., & Díez-Montero, R. (2021). Assessment of hydrodynamics based on computational fluid dynamics to optimize the operation of hybrid tubular photobioreactors. *Journal of Environmental Chemical Engineering*, *9*(5), 105768. https://doi.org/10.1016/j.jece.2021.105768

Carlozzi, P., & Torzillo, G. (1996). Productivity of *Spirulina* in a strongly curved outdoor tubular photobioreactor. *Applied Microbiology and Biotechnology*, *45*(1–2), 18–23. https://doi.org/10.1007/s002530050642

Caspi, R., Altman, T., Billington, R., Dreher, K., Foerster, H., Fulcher, C. A., Holland, T. A., Keseler, I. M., Kothari, A., Kubo, A., Krummenacker, M., Latendresse, M., Mueller, L. A., Ong, Q., Paley, S., Subhraveti, P., Weaver, D. S., Weerasinghe, D., Zhang, P., & Karp, P. D. (2014). The MetaCyc database of metabolic pathways and enzymes and the BioCyc collection of Pathway/Genome Databases. *Nucleic Acids Research*, *42*(D1), D459–D471. https://doi.org/10.1093/nar/gkt1103

Chelf, P., Brown, L. M., & Wyman, C. E. (1993). Aquatic biomass resources and carbon dioxide trapping. *Biomass and Bioenergy*, *4*(3), 175–183. https://doi.org/10.1016/0961-9534(93)90057-B

Cruz, D., Vasconcelos, V., Pierre, G., Michaud, P., & Delattre, C. (2020). Exopolysaccharides from cyanobacteria: Strategies for bioprocess development. *Applied Sciences (Switzerland)*, *10*(11), 3763. https://doi.org/10.3390/APP10113763

Dubois, M., Gilles, K. A., Hamilton, J. K., Rebers, P. A., & Smith, F. (1956). Colorimetric method for determination of sugars and related substances. *Analytical Chemistry*, *28*(3), 350–356. https://doi.org/10.1021/ac60111a017

Fernández, F. G. A., Reis, A., Wijffels, R. H., Barbosa, M., Verdelho, V., & Llamas, B. (2021). The role of microalgae in the bioeconomy. *New Biotechnology*, *61*, 99–107. https://doi.org/10.1016/j.nbt.2020.11.011

Flemming, H. C., & Wingender, J. (2010). The biofilm matrix. *Nature Reviews Microbiology*, *8*(9), 623–633. https://doi.org/10.1038/nrmicro2415

Gaignard, C., Gargouch, N., Dubessay, P., Delattre, C., Pierre, G., Laroche, C., Fendri, I., Abdelkafi, S., & Michaud, P. (2019). New horizons in culture and valorization of red microalgae. *Biotechnology Advances*, *37*(1), 193–222. https://doi.org/10.1016/j.biotechadv.2018.11.014

Goto, T., Aoki, R., Minamizaki, K., & Fujita, Y. (2010). Functional differentiation of two analogous coproporphyrinogen iii oxidases for heme and chlorophyll biosynthesis pathways in the cyanobacterium synechocystis sp. PCC 6803. *Plant and Cell Physiology*, *51*(4), 650–663. https://doi.org/10.1093/pcp/pcq023

Grama, B. S., Agathos, S. N., & Jeffryes, C. S. (2016). Balancing photosynthesis and respiration increases microalgal biomass productivity during photoheterotrophy on glycerol. *ACS Sustainable Chemistry & Engineering*, *4*(3), 1611–1618. https://doi.org/10.1021/acssuschemeng.5b01544

Graverholt, O. S., & Eriksen, N. T. (2007). Heterotrophic high-cell-density fed-batch and continuous-flow cultures of *Galdieria sulphuraria* and production of phycocyanin. *Applied Microbiology and Biotechnology*, *77*(1), 69–75. https://doi.org/10.1007/s00253-007-1150-2

Gross, W., & Oesterhelt, C. (1999). Ecophysiological studies on the red alga *Galdieria sulphuraria* isolated from southwest Iceland. *Plant Biology*, *1*(6), 694–700. https://doi.org/10.1111/j.1438-8677.1999.tb00282.x

Guimarães, B. O., de Boer, K., Gremmen, P., Drinkwaard, A., Wieggers, R., Wijffels, R. H., Barbosa, M. J., & D'Adamo, S. (2021). Selenium enrichment in the marine microalga *Nannochloropsis oceanica*. *Algal Research*, *59*, 102427. https://doi.org/10.1016/j.algal.2021.102427

Hall, D. O., Acién Fernández, F. G., Guerrero, E. C., Rao, K. K., & Grima, E. M. (2003). Outdoor helical tubular photobioreactors for microalgal production: Modeling of fluid-dynamics and mass transfer

and assessment of biomass productivity. *Biotechnology and Bioengineering*, *82*(1), 62–73. https://doi.org/10.1002/bit.10543

Hansson, M., & Hederstedt, L. (1994). Bacillus subtilis HemY is a peripheral membrane protein essential for protoheme IX synthesis which can oxidize coproporphyrinogen III and protoporphyrinogen IX. *Journal of Bacteriology*, *176*(19), 5962–5970. https://doi.org/10.1128/jb.176.19.5962-5970.1994

Janssen, M., Wijffels, R. H., & Barbosa, M. J. (2022). Microalgae based production of single-cell protein. *Current Opinion in Biotechnology*, *75*, 102705. https://doi.org/10.1016/J.COPBIO.2022.102705

Khan, M. I., Shin, J. H., & Kim, J. D. (2018). The promising future of microalgae: Current status, challenges, and optimization of a sustainable and renewable industry for biofuels, feed, and other products. *Microbial Cell Factories*, *17*(1), 36. https://doi.org/10.1186/s12934-018-0879-x

Kim, E. J., Oh, E. K., & Lee, J. K. (2015). Role of HemF and HemN in the heme biosynthesis of *Vibrio vulnificus* under S-adenosylmethionine-limiting conditions. *Molecular Microbiology*, *96*(3), 497–512. https://doi.org/10.1111/mmi.12951

Krishnamurthy, P., Xie, T., & Schuetz, J. D. (2007). The role of transporters in cellular heme and porphyrin homeostasis. *Pharmacology and Therapeutics*, *114*(3), 345–358. https://doi.org/10.1016/j.pharmthera.2007.02.001

Lang, I., Bashir, S., Lorenz, M., Rader, S., & Weber, G. (2020). Exploiting the potential of Cyanidiales as a valuable resource for biotechnological applications. *Applied Phycology*, *3(1)*, 199–210. https://doi.org/10.1080/26388081.2020.1765702

Langley, N. M., Harrison, S. T. L., & van Hille, R. P. (2012). A critical evaluation of CO_2 supplementation to algal systems by direct injection. *Biochemical Engineering Journal*, *68*, 70–75. https://doi.org/10.1016/j.bej.2012.07.013

Lara, A. R., Galindo, E., Ramírez, O. T., & Palomares, L. A. (2006). Living with heterogeneities in bioreactors: Understanding the effects of environmental gradients on cells. *Molecular Biotechnology*, *34*(3), 355–382. https://doi.org/10.1385/MB:34:3:355

Miyatake, T., Moerdijk-Poortvliet, T. C. W., Stal, L. J., & Boschker, H. T. S. (2014). Tracing carbon flow from microphytobenthos to major bacterial groups in an intertidal marine sediment by using an in situ 13C pulse-chase method. *Limnology and Oceanography*, *59*(4), 1275–1287. https://doi.org/10.4319/lo.2014.59.4.1275

de Mooij, T., Janssen, M., Cerezo-Chinarro, O., Mussgnug, J. H., Kruse, O., Ballottari, M., Bassi, R., Bujaldon, S., Wollman, F. A., & Wijffels, R. H. (2015). Antenna size reduction as a strategy to increase biomass productivity: A great potential not yet realized. *Journal of Applied Phycology*, *27*(3), 1063–1077. https://doi.org/10.1007/s10811-014-0427-y

Mulders, K. J. M., Lamers, P. P., Martens, D. E., & Wijffels, R. H. (2014). Phototrophic pigment production with microalgae: Biological constraints and opportunities. *Journal of Phycology*, *50*(2), 229–242. https://doi.org/10.1111/jpy.12173

Nadal-Rey, G., McClure, D. D., Kavanagh, J. M., Cornelissen, S., Fletcher, D. F., & Gernaey, K. V. (2021). Understanding gradients in industrial bioreactors. *Biotechnology Advances*, *46*, 107660. https://doi.org/10.1016/j.biotechadv.2020.107660

Noorman, H. (2011). An industrial perspective on bioreactor scale-down: What we can learn from combined large-scale bioprocess and model fluid studies. *Biotechnology Journal*, *6*(8), 934–943. https://doi.org/10.1002/biot.201000406

Oesterhelt, C., Vogelbein, S., Shrestha, R. P., Stanke, M., & Weber, A. P. M. (2007). The genome of the thermoacidophilic red microalga *Galdieria sulphuraria* encodes a small family of secreted class III peroxidases that might be involved in cell wall modification. *Planta*, *227*(2), 353–362. https://doi.org/10.1007/s00425-007-0622-z

Pang, N., Gu, X., Chen, S., Kirchhoff, H., Lei, H., & Roje, S. (2019). Exploiting mixotrophy for improving productivities of biomass and co-products of microalgae. *Renewable and Sustainable Energy Reviews*, *112*, 450–460. https://doi.org/10.1016/j.rser.2019.06.001

Pereira, J., Mediayati, Y., van Veelen, H. P. J., Temmink, H., Sleutels, T., Hamelers, B., & Heijne, A. (2022). The effect of intermittent anode potential regimes on the morphology and extracellular matrix composition of electro-active bacteria. *Biofilm*, *4*, 100064. https://doi.org/10.1016/j.bioflm.2021.100064

Pierre, G., Delattre, C., Dubessay, P., Jubeau, S., Vialleix, C., Cadoret, J. P., Probert, I., & Michaud, P. (2019). What is in store for EPS microalgae in the next decade? *Molecules*, *24*(23):4296. https://doi.org/10.3390/molecules24234296

Rosello Sastre, R., Csögör, Z., Perner-Nochta, I., Fleck-Schneider, P., & Posten, C. (2007). Scale-down of microalgae cultivations in tubular photo-bioreactors—A conceptual approach. *Journal of Biotechnology*, *132*(2), 127–133. https://doi.org/10.1016/j.jbiotec.2007.04.022

Rouwenhorst, R. J., Frank Jzn, J., Scheffers, W. A., & van Dijken, J. P. (1991). Determination of protein concentration by total organic carbon analysis. *Journal of Biochemical and Biophysical Methods*, *22*(2), 119–128. https://doi.org/10.1016/0165-022X(91)90024-Q

Ruiz, J., Olivieri, G., de Vree, J., Bosma, R., Willems, P., Reith, J. H., Eppink, M. H. M., Kleinegris, D. M. M., Wijffels, R. H., & Barbosa, M. J. (2016). Towards industrial products from microalgae. *Energy and Environmental Science*, *9*(10), 3036–3043. https://doi.org/10.1039/c6ee01493c

Sarian, F. D., Rahman, D. Y., Schepers, O., & Van Der Maarel, M. J. E. C. (2016). Effects of oxygen limitation on the biosynthesis of photo pigments in the red microalgae *Galdieria sulphuraria* strain 074g. *PLoS One*, *11*(2), e0148358. https://doi.org/10.1371/journal.pone.0148358

Stadnichuk, I. N., Rakhimberdieva, M. G., Bolychevtseva, Y. V., Yurina, N. P., Karapetyan, N. V., & Selyakh, I. O. (1998). Inhibition by glucose of chlorophyll a and phycocyanobilin biosynthesis in the unicellular red alga *Galdieria partita* at the stage of coproporphyrinogen III formation. *Plant Science*, *136*(1), 11–23. https://doi.org/10.1016/S0168-9452(98)00088-0

Stuart, R. K., Mayali, X., Lee, J. Z., Craig Everroad, R., Hwang, M., Bebout, B. M., Weber, P. K., Pett-Ridge, J., & Thelen, M. P. (2016). Cyanobacterial reuse of extracellular organic carbon in microbial mats. *The ISME Journal*, *10*(5), 1240–1251. https://doi.org/10.1038/ismej.2015.180

Sun, Y., Shi, M., Lu, T., Ding, D., Sun, Y., & Yuan, Y. (2021). Bio-removal of PtCl62− complex by *Galdieria sulphuraria*. *Science of the Total Environment*, *796*, 149021. https://doi.org/10.1016/j.scitotenv.2021.149021

Sułek, A., Pucelik, B., Kobielusz, M., Barzowska, A., & Dąbrowski, J. M. (2020). Photodynamic inactivation of bacteria with porphyrin derivatives: Effect of charge, lipophilicity, ros generation, and cellular uptake on their biological activity in vitro. *International Journal of Molecular Sciences*, *21*(22), 8716. https://doi.org/10.3390/ijms21228716

Ternes, C. M. (2015). *Metabolic evolution in Galdieria sulphuraria*. Oklahoma State University.

Vis, M. L., Necchi, O. Jr. (2021). *Freshwater red algae: Phylogeny, taxonomy and biogeography*. Springer Cham. https://doi.org/10.1007/978-3-030-83970-3

Weber, A. P. M., Horst, R. J., Barbier, G. G., & Oesterhelt, C. (2007). Metabolism and metabolomics of eukaryotes living under extreme conditions. *International Review of Cytology*, *256*, 1–34. https://doi.org/10.1016/S0074-7696(07)56001-8

Wongluang, P., Chisti, Y., & Srinophakun, T. (2013). Optimal hydrodynamic design of tubular photobioreactors. *Journal of Chemical Technology & Biotechnology*, *88*(1), 55–61. https://doi.org/10.1002/jctb.3898

Zhu, B., Wei, D., & Pohnert, G. (2022). The thermoacidophilic red alga *Galdieria sulphuraria* is a highly efficient cell factory for ammonium

recovery from ultrahigh-NH4+ industrial effluent with co-production of high-protein biomass by photo-fermentation. *Chemical Engineering Journal*, *438*, 135598. https://doi.org/10.1016/j.cej.2022.135598

SUPPORTING INFORMATION

Additional supporting information can be found online in the Supporting Information section at the end of this article.

How to cite this article: Moñino Fernández, P., Vidal García, A., Jansen, T., Evers, W., Barbosa, M., & Janssen, M. (2023). Scale-down of oxygen and glucose fluctuations in a tubular photobioreactor operated under oxygen-balanced mixotrophy. *Biotechnology and Bioengineering*, 120, 1569–1583. https://doi.org/10.1002/bit.28372